New constraints on the magnetic field in cosmic web filaments

Locatelli, N.; Vazza, F.; Bonafede, A.; Banfi, S.; Bernardi, G.; Gheller, C.; ... ; , Shimwell, T.W.

New constraints on the magnetic field in filaments of the cosmic web

Nicola Locatelli[1,2], Franco Vazza[1,2,3], Annalisa Bonafede[1,2,3], Serena Banfi[1,2], Gianni Bernardi[2,4,5], Claudio Gheller[2], Andrea Botteon[6], Timothy Shimwell[6,7]

[1]*Università di Bologna, Dip. di Fisica & Astronomia DIFA, via Gobetti 92, Bologna, Italy*

[2]*INAF – Istituto di Radioastronomia, via Gobetti 92, Bologna, Italy*

[3]*University of Hamburg, Hamburger Sternwarte, Gojenbergsweg 112, 21029 Hamburg, Germany*

[4]*Department of Physics and Electronics, Rhodes University, PO Box 94, Grahamstown, 6140, South Africa*

[5]*South African Radio Astronomy Observatory, Black River Park, 2 Fir Street, Observatory, Cape Town, 7925, South Africa*

[6]*Leiden Observatory, Leiden University, PO Box 9513, 2300 RA Leiden, The Netherlands*

[7]*ASTRON, The Netherlands Institute for Radio Astronomy, Postbus2, 7990 AA Dwingeloo, The Netherlands*

ABSTRACT

Strong accretion shocks are expected to illuminate the warm-hot inter-galactic medium encompassed by the filaments of the cosmic web, through synchrotron radio emission. Given their high sensitivity, low-frequency large radio facilities may already be able to detect signatures of this extended radio emission from the region in between two close and massive galaxy clusters. In this work we exploit the non-detection of such diffuse emission by deep observations of two pairs of relatively close ($\simeq 10$ Mpc) and massive ($M_{500} \geq 10^{14} M_\odot$) galaxy clusters using the LOw-Frequency ARray (LOFAR). By combining the results from the two putative inter-cluster filaments, we derive new independent constraints on the median strength of inter-galactic magnetic fields: $B_{\rm Mpc} < 2.5 \times 10^2$ nG (95% CL). Based on cosmological simulations and assuming a primordial origin of the B-fields, these estimates can be used to limit the amplitude of primordial seed magnetic fields: $B_0 \leq 10$ nG. We advise the observation of similar cluster pairs as a powerful tool to set tight constraints on the amplitude of extragalactic magnetic fields.
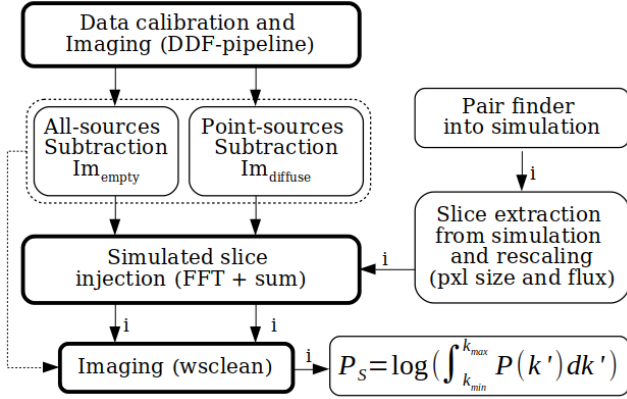
Key words: galaxies: clusters: general - magnetic fields - acceleration of particles

1 INTRODUCTION

At the largest scales of the Universe (≥ 10 Mpc), galaxy groups and clusters are connected by elongated distributions of galaxies called filaments and sheets which are believed to be also permeated by diffuse gas, and possibly by magnetic fields. Until now, a straightforward and direct detection of inter-galactic medium (IGM) and magnetic field (IGMF) has been prevented by the very low density of the plasma ($n_{\rm IGM} \leq 10^{-4}$ cm^{-3}) and its relatively low temperature ($T_{\rm IGM} \leq 10^7$ K). However, increasing evidence (Nicastro et al. 2018; Macquart et al. 2020) is recently confirming the long-lived expectations for the warm-hot gas phase of the IGM (WHIM, with $T_{\rm WHIM} \sim 10^5 - 10^7$, $n_{\rm WHIM} \sim 10^{-5} - 10^{-4}$) to contain up to half of the baryon content at low redshift (Cen & Ostriker 1999; Davé et al. 2001).

Accretion shocks are believed to reside along and within the filaments of the cosmic web as well as at the outskirts of galaxy clusters. These shocks are expected to amplify the magnetic fields and to accelerate particles up to relativistic energies (Ryu et al. 2008). Their presence might then enable the detection of the WHIM through its synchrotron emission signature at radio wavelengths, and indeed the direct observation of the tip of the iceberg of this diffuse emission has already been discovered at radio frequencies (Govoni et al.

2019; Botteon et al. 2020a). In these few cases the plasma conditions are still hotter and denser than what expected for the WHIM and the detected emission lays within the clusters virial radii. Further works in this direction will be helped in the near future by the promising new and upcoming radio facilities (ngVLA, MeerKAT, SKA-mid) and especially at very low frequencies (LOFAR, MWA, SKA-low) where the emission should be brighter up to further out the clusters virial radii thanks to the expected spectral behaviour as $S_\nu \propto \nu^{-1}$ with respect to frequency ν (Vazza et al. 2015). A way to overcome sensitivity limitations is to quantify the Faraday effect induced by magneto-ionized plasma along the line of sight to a polarized background radio source and build a tomography of the WHIM by means of a grid of background sources (see Akahori et al. 2014; Vacca et al. 2016). A thorough exploitation of this method currently suffers from the lack of large and dense grids of polarized sources, however it is expected to provide important results thanks to the upcoming radio facilities (Locatelli et al. 2018). Complementary, recent upper limits on the IGMF intensity and scale have been derived from the cross-correlation of diffuse radio synchrotron emission with the underlying galaxy distribution (Vernstrom et al. 2017; Brown et al. 2017) or by cross-correlating the difference in rotation measures of physically related pairs of extended radio galaxies, compared with

Data calibration and
Imaging (DDF-pipeline)

All-sources Subtraction $\mathrm{Im_{empty}}$ Point-sources Subtraction $\mathrm{Im_{diffuse}}$

Pair finder into simulation

Slice extraction from simulation and rescaling (pxl size and flux)

Simulated slice injection (FFT + sum)

Imaging (wsclean) $P_S = \log\left(\int_{k_{min}}^{k_{max}} P(k')dk'\right)$

Figure 1. Diagram of the method outlined in Sec. 2. Thick boxes highlight the most computationally expensive steps. Links labelled with the letter "i" are computed iteratively over the simulated pairs.

the one derived from randomly paired and close lobes (Vernstrom et al. 2019; O'Sullivan et al. 2020; Stuardi et al. 2020).

Why is it important to assess the IGMF properties in the cosmic web at late times? The magnetic fields in galaxies and galaxy clusters, commonly observed today, arise from strong amplification from efficient MHD small-scale mechanisms (Ryu et al. 2008) which are responsible of a fast saturation of the fields, thus erasing information on their initial conditions, and in turn of their origin (Beresnyak & Miniati 2016). Instead, in the WHIM environment, the amplification of primordial magnetic fields is found in simulations to be mainly driven by the field compression as its lines freeze into the plasma plus the contribution of small scale shocks. These mechanisms do not bring the field to saturation and provide a tool of assessing the history and original conditions of the field by means of the level of magnetisation observed today (Vazza et al. 2014, 2015; Donnert et al. 2018). For the above reasons it is crucial to constrain the magnetic field in the WHIM in order to determine the original scenario for the large scale magnetic field origin and evolution in the Universe.

Cosmological MHD simulations predict the intensity of the IGMF at low redshift to range within 1 and 100 nG (Dolag et al. 1999; Brüggen et al. 2005; Vazza et al. 2017). In this paper we introduce a novel method for a robust inference of an upper limit on the initial B_0 and current B values of the IGMF within the large-scale filaments of the cosmic web. The method explores the amount of diffuse emission detected at 144 MHz with the LOw Frequency ARray (LOFAR) telescope along the direction connecting two different pairs of galaxy clusters. We outline the method used to explore the upper limits on the IGMF into cosmological filaments in the following Sec. 2; we show its results in Sec. 3 and discuss their assumptions and implications in Sec. 4; we draw our conclusions in Sec. 5. Throughout this work we assumed a ΛCDM cosmological model, with baryonic and dark matter and dark energy density parameters $\Omega_{\mathrm{BM}} = 0.0455$, $\Omega_{\mathrm{DM}} = 0.2265$, $\Omega_{\Lambda} = 0.728$ respectively and a Hubble constant $H_0 = 70.2 \mathrm{km\,s^{-1}\,Mpc^{-1}}$.

2   METHOD

In order to look for large scale emission from the cosmic web, we observed pairs of galaxy clusters and the putative inter-cluster filaments connecting them. The cluster pairs were selected from the

MCXC Meta-Catalog of X-Ray Detected Clusters of Galaxies[1] by applying cuts in declination ($\delta \geq 10\,\mathrm{deg}$), redshift ($z \leq 0.3$) and maximum angular separation ($\theta \leq 5\,\mathrm{deg}$). These values are tailored to the proposed LOFAR observations. The two most promising pairs that, according to cosmological simulations, maximise the probability of a physical connection between the clusters in terms of total mass and separation (real and projected), were proposed and observed at the LOFAR during Cycle 9 (Proposal Id:LC9_020). The most important properties of the two observed pairs of clusters are given in Tab.1.

In a nutshell, after calibrating, imaging and removing contaminating sources from the LOFAR data, we quantify the confidence of having observed (or not) diffuse emission from the inter-cluster filaments by injecting simulated diffuse emission produced by large scale ($\geq$Mpc) accretion shocks, into the original radio visibility data (uvw) for a large ($O(100)$) subset of simulated filaments/cluster pairs and by imaging them as done for the real observations.
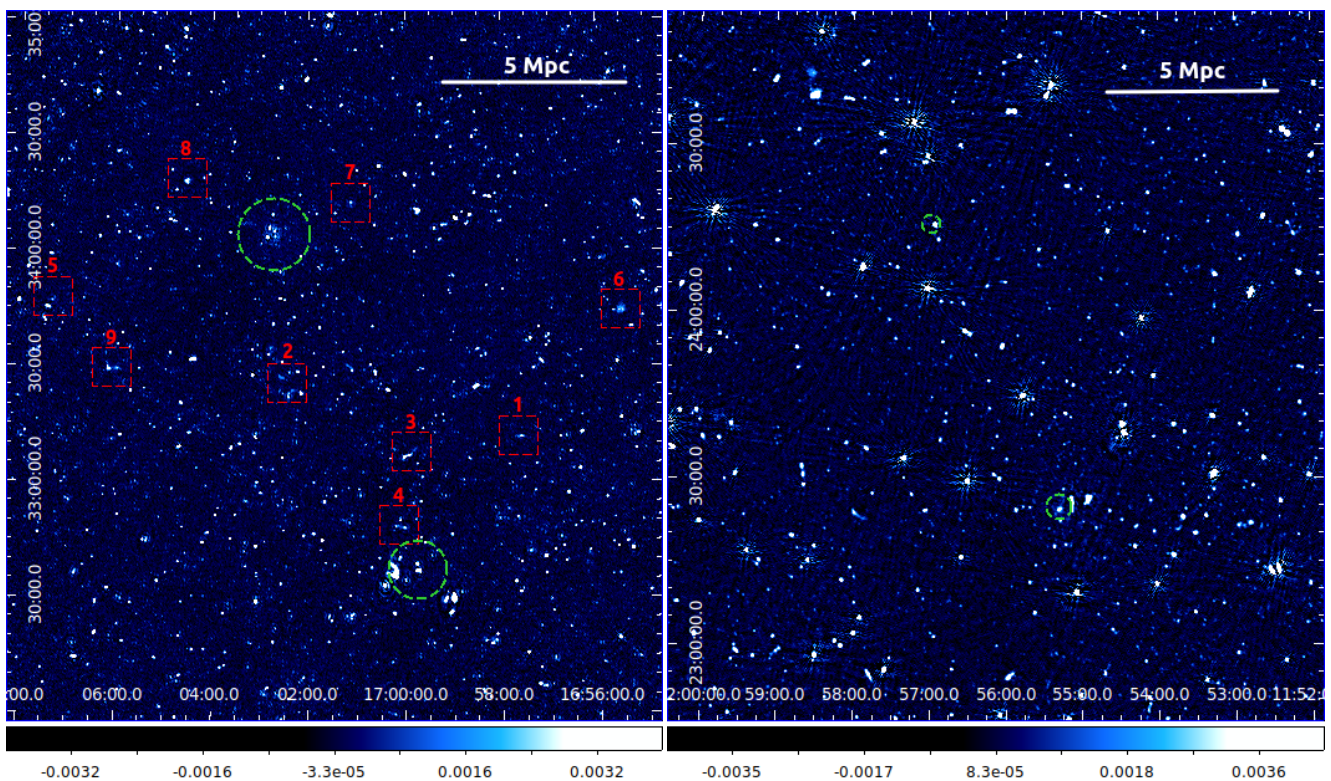
In this section we provide further details on the analysis performed on the actual observations, the simulated data set prepared for the injection and the injection procedure (also sketched by the diagram in Fig. 1).

2.1   LOFAR radio observations

We observed the two cluster pairs RXCJ1659.7+3236-RXCJ1702.7+3403 (hereafter RXC_J1659-J1702) and RXCJ1155.3+2324-RXCJ1156.9+2415 (hereafter RXC_J1155-J1156) using LOFAR. The fields containing these two targets were co-observed together with two pointings of the LOFAR Two-meter Sky Survey (LoTSS; Shimwell et al. 2017) taking advantage of the multi-beam capabilities of LOFAR. The observing setup of our observations thus follows that of LoTSS, namely 8 hr on-source time book-ended by two 10 min scans on the flux density calibrator in the frequency range 120-168 MHz using LOFAR in HBA_DUAL_INNER mode (see Shimwell et al. 2017, for details). A first calibration and imaging run was performed adopting the pipelines developed to analyze LoTSS pointings (Shimwell et al. 2017, 2019), that aim to correct both for direction-independent and direction-dependent effects exploiting PREFACTOR (Williams et al. 2016; van Weeren et al. 2016; de Gasperin et al. 2019), KILLMS (Tasse 2014a,b; Smirnov & Tasse 2015), and DDFACET (Tasse et al. 2018). In particular, we made use the improved version of the direction-dependent data reduction pipeline (v2.2[2], the same used for the forthcoming second LoTSS data release DR2, Shimwell et al. in preparation) to produce images of the full LOFAR field-of-view at the central frequency of 144 MHz at high (6″) and low resolution (20″, shown in Fig. 2) using a Briggs weighting scheme (robust=-0.5). We refer the reader to Tasse et al. (submitted) for a thorough description of the steps performed by the pipeline. Using the sky models derived from the pipeline, we subtracted the sources from the uv-data in two different fashions: either we subtracted all sources (by means of their clean components) found in the high and low resolution maps or we subtracted all sources detected in the high resolution image. The model components were determined during the high and low resolution images deconvolution making use of the PYthon Blob Detector and Source Finder (PYBDSF; Mohan & Rafferty 2015). The subtraction of the model components was performed

---

[1] http://heasarc.gsfc.nasa.gov/W3Browse/all/mcxc.html
[2] https://github.com/mhardcastle/ddf-pipeline

Figure 2. LOFAR low-resolution (20″) images at 150 MHz of the cluster pairs RXC_J1659-J1702 (left panel) and RXC_J1155-J1156 (right panel). The dashed circles are centered on the clusters and have corresponding radius R_{500}. The red dashed boxes in the left panel have been zoomed in Fig. 8. We indicated the 5 Mpc unit at the redshift of the pairs $z = 0.10, 0.14$ (left and right panels). Colorbars are in units of Jy beam^{-1}.

in the visibility domain, corrupting the model components by the direction-independent antenna gains obtained from the calibration. We then produced dirty images from the subtracted data. The images include the residual contribute to the surface brightness resulting from model approximation plus artefacts associated with imperfect model and solutions ($\mathrm{Im}_{\mathrm{empty}}$) plus patches of faint extended emission in the case in which only sources from the high resolution model were subtracted ($\mathrm{Im}_{\mathrm{diffuse}}$). The subtracted (dirty-)images $\mathrm{Im}_{\mathrm{empty}}$ at low resolution (20″) have a rms noise floor of ~ 160 and $240\ \mu\mathrm{Jy\,beam}^{-1}$ for the two fields, respectively. The noise difference is consistent with the amount of flagged (i.e. discarded) data in the two observations.

2.2 Cosmological simulations

We extracted the simulated inter-cluster filaments from the suite of simulations of the cosmic web properties described in Vazza et al. (2019) performed with the cosmological MHD code ENZO[3] (Bryan et al. 2014). They consist in a comoving 100^3 Mpc^3 box with a uniform grid of 2400^3 cells (and 2400^3 dark matter particles) with linear (comoving) resolution of 41.6 kpc per cell and dark matter mass $m_{dm} = 8.62 \times 10^6\ M_\odot$ per dark matter particle. Magnetic fields have been initialized at $z = 45$ as a uniform background of of $B_0 = 0.1$ nG and evolved at run-time using the MHD method of Dedner (Dedner et al. 2002). We note that a uniform initial magnetic field here would correspond to a scale-invariant spectrum in the models used for Cosmic Microwave Background (CMB) analysis

(Aghanim et al. 2019; Paoletti & Finelli 2019). We also note that the run was non-radiative and did not include any treatment for star formation or feedback from active galactic nuclei (AGN). To a first approximation, these processes are not very relevant for the radio and X-ray properties of the peripheral regions of galaxy clusters and filaments (Vazza et al. 2017), which are our main focus.

2.3 Synchrotron emission model for cosmic shocks

We produced synthetic maps of synchrotron radio emission assuming that diffusive shock acceleration (DSA, e.g. Kang et al. 2012 and references therein) accelerates a small fraction of thermal electrons swept by structure formation shocks up to relativistic energies, as in Vazza et al. (2019). We computed the radio emission from electrons in the downstream cooling region of shocks using the model of Hoeft & Brüggen (2007) and based on the shocks identified in post-processing in the simulation. The total acceleration efficiency at shocks, $\xi_e(\mathcal{M})$ (with $\mathcal{M}$ the Mach number) is assumed to be the combination of two variables: the kinetic energy flux dissipated onto the acceleration of cosmic rays, $\psi(\mathcal{M})$, and the fraction going into electron acceleration, ξ'_e, giving $\xi_e(\mathcal{M}) = \xi'_e \cdot \psi(\mathcal{M})$. Following Hoeft & Brüggen (2007), the radio emission in the downstream of each shock is directly linked to the power-law energy distributions $N_\gamma \propto \gamma^{-p}$ of electrons accelerated by the shock front during a cooling time, through the integrated radio spectrum of $I(\nu) \propto \nu^{-s}$, where $s = (p-1)/2 + 1/2$, with $p = 2(\mathcal{M}^2+1)/(\mathcal{M}^2-1)$. With this approach and for the range of $\mathcal{M} \gg 5$ shocks usually found within and around simulated filaments, as well as for the $\leq \mu$G magnetic fields in filaments (e.g. Vazza et al. 2017), the radio emission thus scales as $I(\nu) \propto \xi_e B^2 \nu^{-2}$. The baseline model used in this work

Cluster name	R.A. [h,m,s]	Dec. [°,′,″]	z	L_X [erg/s]	M_{500} [$M_\odot$]	R_{500} [Mpc]	$d_{3D}/(R_1+R_2)$	angular separation [°]	$L_{\rm fila}$ [Mpc]
RXCJ1155.3+2324	11 55 18	+23 24 27	0.142	$6.04 \cdot 10^{44}$	$5.60 \cdot 10^{14}$	1.19	4.88	0.93	8.25
RXCJ1156.9+2415	11 56 58	+24 15 29	0.139	$1.50 \cdot 10^{44}$	$2.40 \cdot 10^{14}$	0.90	4.88	0.93	8.25
RXCJ1659.7+3236	16 59 44	+32 36 49	0.101	$1.12 \cdot 10^{44}$	$2.04 \cdot 10^{14}$	0.87	7.76	1.57	10.13
RXCJ1702.7+3403	17 02 42	+34 03 43	0.095	$4.04 \cdot 10^{44}$	$4.49 \cdot 10^{14}$	1.01	7.76	1.57	10.13

Table 1. Main parameters of the two pairs of galaxy clusters observed in this work, based on the MCXC Meta-Catalog of X-Ray Detected Clusters of Galaxies (Piffaretti et al. 2011). In the last three columns, we give the 3-dimensional distance of between the two cluster centres, normalized by the radius of the two clusters), the angular separation of the two cluster centres, and the 3-dimensional length of the filament (considering the cluster to cluster distance).

assumes $\xi_e = 10^{-2}$, which is in line with DSA expectations for the maximal acceleration efficiency of relativistic electrons by strong shocks (e.g. Hoeft & Brüggen 2007; Kang et al. 2012; Bykov et al. 2019a), also is also compatible with the modelling of supernova remnants (e.g. Uchiyama et al. 2007; Bykov et al. 2019b). However, we shall notice that in typically weak ($\mathcal{M} \leq 4$) shocks leading to radio relics in galaxy clusters (e.g. van Weeren et al. 2019), the acceleration efficiencies implied by the observed relic radio fluxes can be much larger ($\xi_e \sim 0.1-1$, see e.g. Stuardi et al. 2019 and Botteon et al. 2020b), thus making our maximal value of $\xi_e = 10^{-2}$ a conservative one. We notice however that very recent particle-in-cell (PIC) simulations (albeit in 1D and with some limiting assumptions) have derived a $\sim 5\%$ electron acceleration efficiency by strong shocks (Xu et al. 2020). For the remainder of the paper, the reader must thus bare in mind that our limits on $B_{\rm Mpc}$ must be accordingly rescaled if a different value of ξ_e is adopted.

Fig. 3 gives an example of filaments connecting a massive cluster to other groups in its surrounding, in an ENZO cosmological simulation. A small but significant fraction of radio emission from shocks running on filaments connecting some of the pairs (e.g. M1-M2, M1-M4 and M1-M6 in Fig. 3) is above the detection threshold in LOFAR-HBA for our baseline model. In all cases, the detectable emission comes from relatively small and localised patches, extended a few $\sim 10'$ at most, with irregular shapes. Detecting the radio signal from cosmic filaments is indeed made challenging by the fact that the detectable fraction is just the tip of the iceberg of the wider "radio cosmic web", which makes a morphological classification of the emission often ambiguous. Indeed advanced Deep Learning techniques have been proposed for the detection of the cosmic web in next radio surveys (Gheller et al. 2018). In the following section we use this model to constrain the amplitude of the $\xi_e B^2$ combination based on our real LOFAR observations.

2.4 Generation of a mock catalog of inter-cluster filaments

For each observed pair of clusters we selected simulated pairs holding individual cluster masses $M_{500} > 10^{13} M_\odot$ and linear (comoving) and projected angular distance of clusters in the pair within 20% deviation from the values of the observed pair (see the last and second-last columns in Tab. 1). We obtained 125 simulated cluster pairs selected for RXC_J1659-J1702 and 103 pairs for RXC_J1155-J1156. The cluster pairs selected above mirror the separation selection criteria of our observations but include less massive clusters that may not involve a physical connection within one pair. We thus analysed in addition a sub-sample of high-mass clusters ($M_{500} > 3 \times 10^{13} M_\odot$) for which a physical connection and the presence of a inter-cluster filament was verified either manually and through a high temperature cut $T_{\rm WHIM} > 10^5$ K of the WHIM within the inter-cluster filament. We refer to this sub-sample as *best*.

Taken a simulated cluster pair, a box has been drawn and extracted along the direction connecting the pair. The box has been rescaled to match the angular scale and comoving transverse distance indicated by the pixel size and redshifts of the observed clusters, and the intensity of synchrotron emission has been scaled to match its luminosity distance by conserving the total power (see the lower left panel in Fig. 4 for an example).

The flux density has been also multiplied by a constant factor $f_B \equiv \xi_e [B_0/(0.1\,{\rm nG})]^2$. Under the assumption that the amplification of the magnetic field into the simulated filaments is affected by negligible small scale dynamo (Ryu et al. 2008) and that it is thus mainly driven by the adiabatic compression of the magnetic field lines following from flux freezing[4] into the plasma condensing during structure formation (Vazza et al. 2017), the magnetic field B in the simulation is scalable with respect to B_0 and in turn the synchrotron emissivity is scalable with respect to $f_B \propto \xi_e B_0^2$.

2.5 Injection of model radio emission into real LOFAR images

The rescaled simulated image of each mock pair of galaxy clusters was injected into the source-subtracted Measurement Set (MS), following the procedure sketched in Fig.1. In detail, each rescaled image was first Fourier-transformed, then written into the MS and finally added to the visibilities of the source-subtracted sky using WSCLEAN (Offringa et al. 2014). We note that such injection does not take into account direction dependent effects that may act on the MS radio data. With the same software, the resulting data-set was imaged and deconvolved with a $20''$ uv-taper and synthetised beam, and Briggs weighting scheme (Briggs 1995) with robust=-0.25 and 2000 minor cycles (see Fig. 4 for output examples). For realistic values of the normalisation parameter f_B, the detectable emission is fragmented into small and sparse patches, associated with shocks internal to filaments. Therefore, we resort to statistical methods to assess the likelihood of each mock image to be compatible with our observed LOFAR fields. We computed the integral of the image power spectrum $P_S \equiv \log_{10}\left(\int_{k_{\rm min}}^{k_{\rm max}} P(k')\,dk'\right)$ where $P(k')$ is the power spectrum and $k_{\rm min}$ and $k_{\rm max}$ are determined by the image and beam size respectively (see Fig. 9 for an example). The sky model subtraction can leave bright residual artefacts depending on the goodness of the model used. These residuals can be as bright as $\sim 0.1\,{\rm Jy\,beam^{-1}}$ around point-like sources and they may dominate the integral of the image power spectrum P_S. A zero-padding mask was manually generated for each pair of clusters in order to exclude those artefact from the computation of P_S in all images.

---

[4] the magnetic flux through a closed loop C enclosing the surface $\mathbf{S}$ is simply $\Phi_{\rm B} = \int_S \mathbf{B} \cdot d\mathbf{S}$, valid for ideal plasma conditions
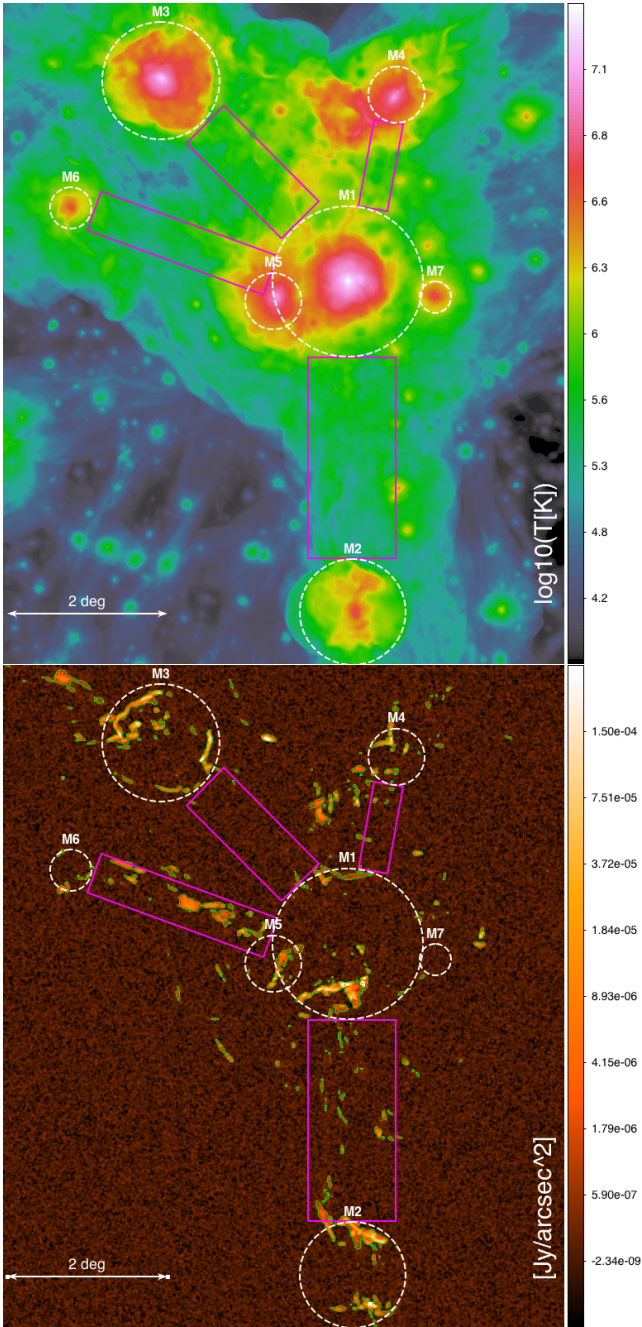
Figure 3. Example of mean gas temperature (top) and mock LOFAR-HBA observation (bottom, $\nu = 140$ MHz, $25''$ resolution, 250μJy beam^{-1} noised added) from the ENZO simulation. Circles mark the virial region of clusters, magenta rectangles mark filaments. The detectable emission ($\geq 3\sigma$) is marked with green contours. The cluster field is placed at $z = 0.1$.

3   RESULTS

From the cumulative probability distributions of the statistic P_S resulting from all the source injections, we can access how likely is for a model to provide an expected value smaller than the one recovered from the observations. From the image Im$_{empty}$, a 2.5 deg $\times$ 2.5 deg square centered on the axis of the cluster pair, in which all the sources (point-like plus extended) have been subtracted, we compute $\tilde{P}_S \equiv P_S(\text{Im}_{empty})$. $\tilde{P}_S$ corresponds to the total power in Im$_{empty}$ distributed over all scales from twice the beam size (k_{min})

up to half the image size (k_{max}). All images resulting from injection thus have P_S equal or larger than the one computed for Im$_{empty}$ (red dotted lines in Fig. 5). The statistic P_S resulting from the image in which diffuse emission was not subtracted Im$_{diffuse}$ are indicated by the blue dashed vertical lines in Fig. 5. Total of 3.1, 5.7 mJy of diffuse emission were found in Im$_{diffuse}$ in excess of Im$_{empty}$ for RXC_J1659-J1702 and RXC_J1155-J1156 respectively. We outlined the probabilities for the different models in Tab. 2. The table reports also results from injection performed in the image plane (instead that in the uvw-plane) found in general to produce different probabilities of non-detection with respect to injection through the uvw-plane. We discuss this alternative method in Sec. 4.

The overall probability of a magnetic field model is simply the product of the probabilities (of the model to produce lower statistics) of the two cluster pairs, since the experiments have been run independently on each pair. We compute these probabilities in the "all" bottom lines in Tab. 2. A model is more likely to be discarded, when its probability of having a smaller P_S than in our LOFAR observations is very small (or very high alternatively).

Our main results can be so summarised:

- the primordial scenario with a seed magnetic field of $B_0 \simeq$ 30 nG has a small probability $P(< P_S) \simeq 0.05$ of explaining the small power excess in our observation of the RXC_J1659-J1702 and RXC_J1155-J1156 pairs, we then reject it with a confidence level (CL) of $> 95\%$.

- the models with a lower seed magnetic fields $B_0 < 30$ nG yield non-negligible (≥ 0.1) probabilities to produce a statistic equal to (o smaller than) the one observed.

- by tightening the constraint on individual cluster masses and on the presence of a inter-cluster filament connecting the clusters, the model with $B_0 = 10$ nG can be rejected as well with CL$> 95\%$.

- If any of the patches of diffuse emission observed is produced by shocks in the WHIM, then the $B_0 = 0.1$ nG model is highly disfavoured, as it is basically unable to produce any detectable emission (i.e the probability in Tab.2 of this model to produce less diffuse emission than what found in Im$_{empty}$ are always ≈ 1; we note that they have not been plotted in Fig. 5). Although we do not reject this scenario, we consider it implausible (see Sec. 4).
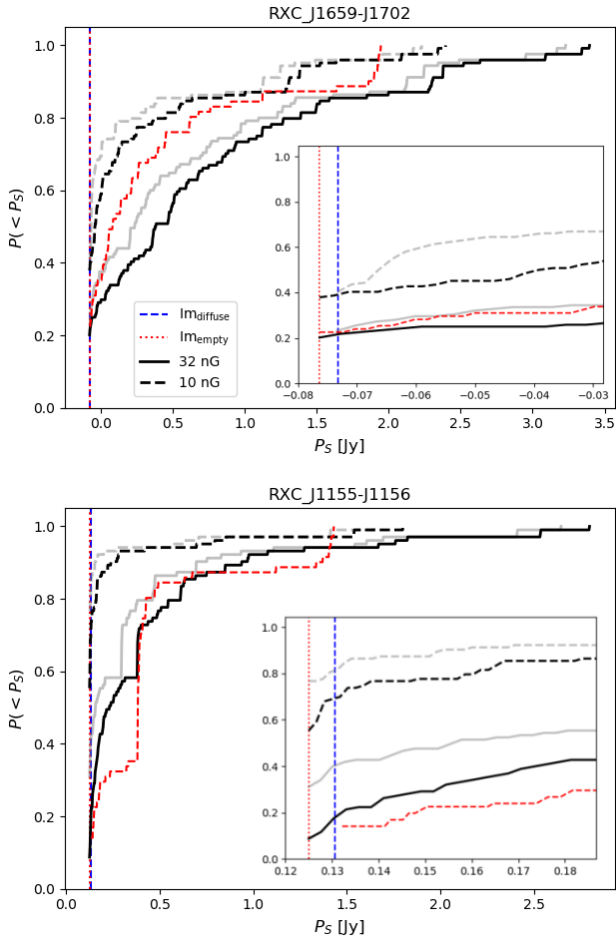
4   DISCUSSION

From the original simulation holding $B_0 = 0.1$ nG, we extract the probability distribution functions (PDF) of the magnetic field values B_{Mpc} across the mock filaments selected according to the properties of the observed cluster pairs. We plot the resulting PDF(log B_{Mpc}) in Fig. 6. Given the expected lack of dynamo amplification in the WHIM, the magnetic field distributions PDF(log B_{Mpc}) corresponding to the other B_0 models can easily be rescaled linearly with the input seed field. We find a skewed distribution encompassing $B_{Mpc} = 1.0 - 7.4$ nG values (90% confidence range) with median $B_{Mpc} = 2.5$ nG (equivalent to log $B_{Mpc} = -8.6$ nG) for the full sample. We note that the value of the magnetic field that produces the simulated synchrotron emission lays in the high part of the B_{Mpc} distribution, as can be seen from the emission-weighted B_{Mpc} distribuion in Fig. 6. We also give in Fig.7 the average profiles of mass-weighted magnetic field strength for all simulated filaments extracted with the procedure above, for the two cluster pairs. On average, the profile of magnetic field is very uniform across $10 - 20$ Mpc, with an average magnetic field along the line of
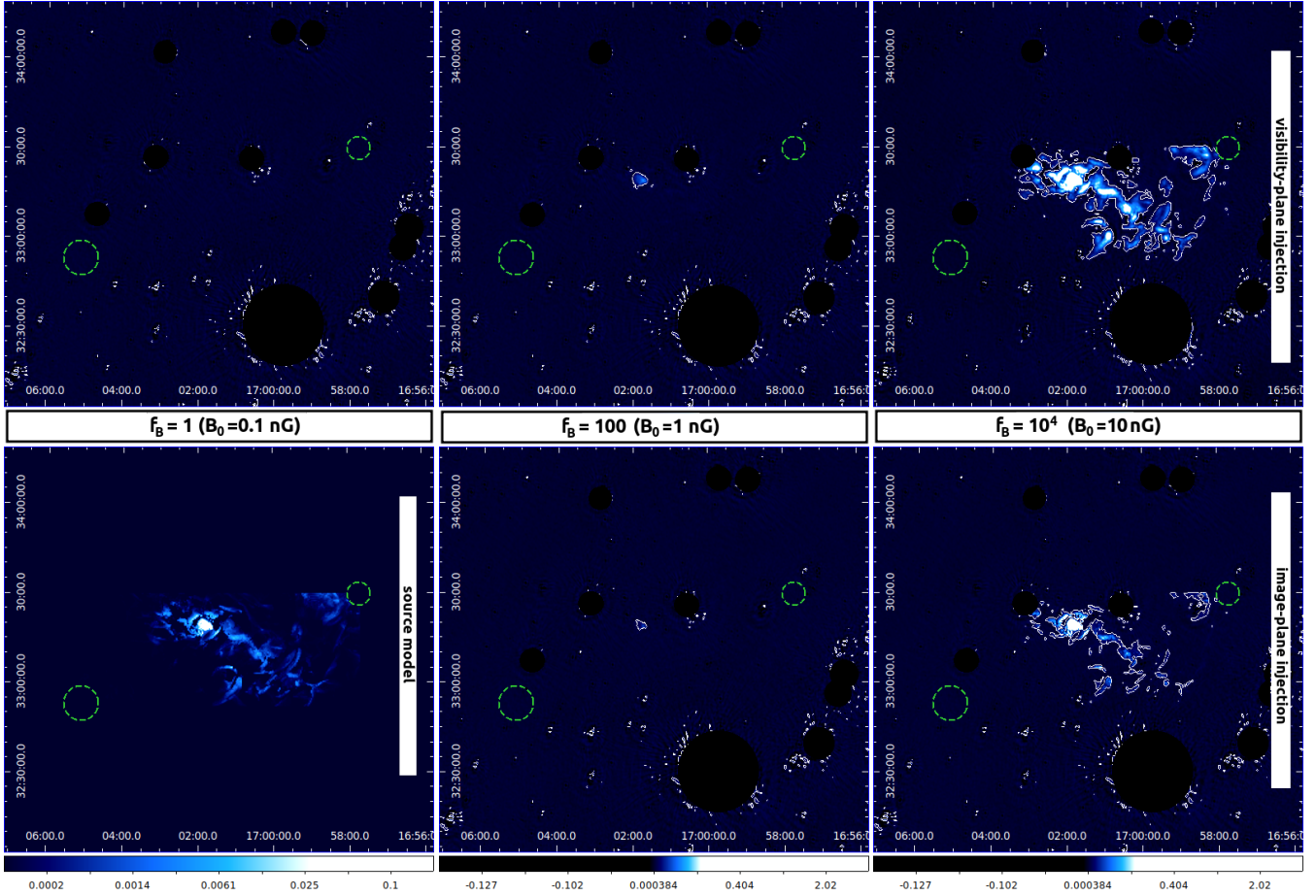
Figure 4. Example of source injection: the model of diffuse emission between a pair of simulated galaxy clusters (masked within their R_{200}, indicated by the green dashed circles) found in the simulation with $B_0 = 0.1$ nG (lower left panel) is multiplied by a factor $f_B = 1$, 10^2, 10^4 imaged and masked after being injected into the source-subtracted sky visibilities (upper left, upper central and upper right panels respectively), or it is injected through the image-plane (lower central and lower right panels for $f_B = 10^2$, 10^4 repectively). The image with $f_B = 1$ in the upper left panel, due to the very low brightness of the model with $B_0 = 0.1$ nG, results to be equal to the source-subtracted sky image $\mathrm{Im_{empty}}$, in which the only features are the residuals from the source subtraction process wich fall outside the masks. The white contours have been set to 5 times the rms value in $\mathrm{Im_{empty}}$.

name	f_B	B_0 [nG]	uvw-plane		image-plane	
			$\mathrm{Im_{empty}}$	$\mathrm{Im_{diffuse}}$	$\mathrm{Im_{empty}}$	$\mathrm{Im_{diffuse}}$
RXC_J1659-J1702	1	0.1	1	1	1	1
	10^2	1	0.98	0.98	0.86	1
	10^4	10	0.38	0.39	0.40	0.40
*best			0.23	0.23	0.24	0.24
	10^5	30	0.20	0.22	0.23	0.23
RXC_J1155-J1156	1	0.1	1	1	1	1
	10^2	1	0.77	0.96	0.85	0.97
	10^4	10	0.55	0.69	0.77	0.81
*best			0.14	0.14	0.18	0.18
	10^5	30	0.09	0.18	0.31	0.40
all	1	0.1	**1**	1	1	1
	10^2	1	0.75	0.94	0.73	0.97
	10^4	10	0.21	0.21	0.31	0.32
*best			**0.03**	0.03	0.04	0.04
	10^5	30	**0.02**	0.04	0.07	0.09

Table 2. Probabilities of obtaining a statistic P_S lower than the one observed in $\mathrm{Im_{empty}}$ and $\mathrm{Im_{diffuse}}$, computed from source injection performed in the uvw-plane and in the image-plane. We highlight with bold face the values used to derive the limits on B and B_0 in this work.
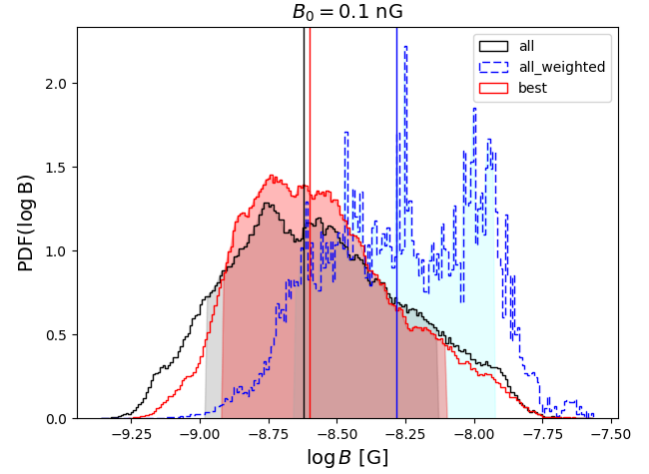
Figure 6. PDFs of the log B_{Mpc} field across all the simulated filaments in the $B_0 = 0.1$ nG model, for all the pairs in the mock sample (black line) and for the *best* sub-sample (red line). The dashed blue lines show the log B_{Mpc} distribution from all pairs weighted over the pixels emissivity. The filled hatched areas encompass the $10 - 90$ percentile ranges. The vertical solid lines show the median of the distributions.
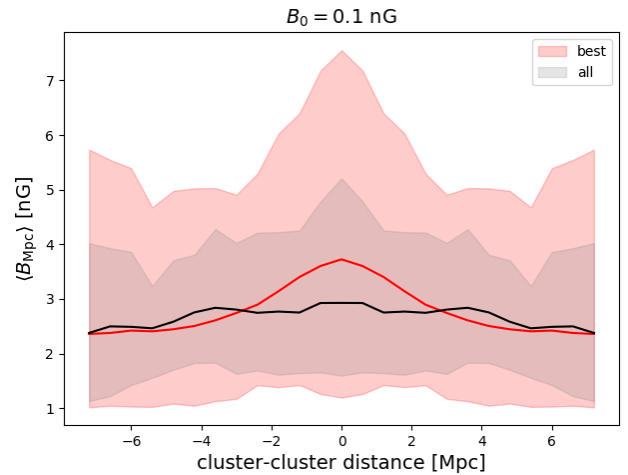
Figure 7. Average profile of mass-weighted magnetic field strength for all inter-cluster filaments extracted to resemble the two cluster pairs studied in this work and for the *best* sub-sample, resulting from the $B_0 = 0.1$ nG model. The solid lines give the median value of the two samples (with 235 and 142 objects, respectively) while the filled areas encompass the $10 - 90$th percentiles of the distributions.

Figure 5. Probability distributions of finding statistics P_S smaller than the values set by the cluster pair RXC_J1659-J1702 (upper panel) and RXC_J1155-J1156 (lower panel) for scenarios with B_0 as labelled. The vertical lines show the P_S values computed without any injection from $\mathrm{Im}_{\mathrm{empty}}$ (red dotted), $\mathrm{Im}_{\mathrm{diffuse}}$ (blue dashed) Black and grey lines show results for source injection performed respectively in the visibility and image domains. The insets show a zoom on the bins where $P(< P_S) \equiv P(< \tilde{P}_S)$.

sight for these objects of $\sim 2 - 3$ nG and a tail of rare and massive filaments that can reach ~ 10 nG.

To interpret the results provided in Fig. 5 and Tab. 2, we postulate three different assumptions that exploit the different type of source-subtraction performed in the analysis, and that can be used to derive different priors from our data (vertical lines in Fig. 5):

I : none of the residual diffuse emission after the point-like source subtraction ($\mathrm{Im}_{\mathrm{empty}}$) is produced by the shocked cosmic web;

II : all of the residual diffuse emission in excess of $\mathrm{Im}_{\mathrm{empty}}$ (i.e. $\mathrm{Im}_{\mathrm{diffuse}}$) is produced by the shocked cosmic web;

III : at least some of the excess diffuse emission present in $\mathrm{Im}_{\mathrm{diffuse}}$ comes from the cosmic web.

Provided that we can fix the ξ_e acceleration efficiency at strong shocks ($\xi_e \approx 10^{-2}$), the assumption that none of the observed emission comes from cosmological shocks (I), produces in principle tighter constraints on B_{Mpc} (and B_0), since $P(P_S(\mathrm{Im}_{\mathrm{empty}})) \leq P(P_S(\mathrm{Im}_{\mathrm{diffuse}}))$ always. In practice, the constraints are just slightly tighter due to the small amount of diffuse emission found into $\mathrm{Im}_{\mathrm{diffuse}}$ with respect to $\mathrm{Im}_{\mathrm{empty}}$. Thus, under the first hypothesis

that we did not observe the cosmic web emission, by scaling the B_{Mpc} distribution to match the $B_0 = 30$ nG model (i.e. a factor $\times 300$) we infer an upper limit to the current median IGMF into filaments of $B < 0.8 \, \mu$G with 95% confidence (the same confidence level that applies to the rejection of $B_0 \geq 30$ nG models of the primordial magnetic field scenario). By considering the *best* sub-sample of cluster pairs with higher masses and connected by an inter-cluster filament we can further improve the constraints on B by rejecting with a CL> 95% also the $B_0 = 10$ nG model. Equivalently, this limit also sets $B_{\mathrm{Mpc}} < 0.25 \, \mu$G with the same CL. In principle we can not exclude that the observed pairs do not hold an inter-cluster filament, however this probability has been accessed in several works and amounts to $\leq 20\%$ for the mass range

and separation of these two pairs of clusters (Colberg et al. 2005; Locatelli et al. 2018).

The assumption that the excess diffuse emission present in $Im_{diffuse}$ with respect to Im_{empty} is entirely due to shocked plasma of the WHIM (hypothesis II) can be readily tested by looking in detail at the diffuse emission patches which have been detected. In Fig. 8 we present close-up clippings of the diffuse patches found close to the pair RXC_J1659-J1702, taken from the low resolution LOFAR images (before source-subtraction). They are meant to help in assessing the nature of some of the diffuse emission, indicated by the dashed red circles in the panels of Fig. 8. We also marked with green X symbols the position of sources already known from the VLA Faint Images of the Radio Sky at Twenty-centimeters (FIRST) survey (Becker et al. 1995). Most of the diffuse emission is plausibly linked to the lobes of radio-galaxies already detected at higher frequencies. Panel 7 (panels are numbered from 1 to 9 from left to right, top to bottom) shows what look like either a radio lobe or an artefact linked to a low-frequency point source. Panels 2, 5 and 6 instead show diffuse emission which is neither obviously linked to radio galaxies, nor to deconvolution artefacts. However, looking at their coordinates, sources 5 and 6 are found to be distant from the axis connecting the clusters, albeit within the imaged portion of the sky around the pair (see also Fig. 2). This makes their physical connection to the putative inter-cluster filament unlikely, even if the shocked cosmic web is expected to fill the space inbetween clusters in a non-trivial way, as shown in Fig.3. Furthermore, the point-like source embedded into the diffuse emission in panel 6 is also found to be at a different redshift with respect to the cluster pair. For the above reasons, these patches can hardly be used in the comparison with the simulated inter-cluster filaments. The diffuse patches in panel 2 instead embed optical galaxies with redshift $z = 0.087$, 0.093, consistent with the cluster pair $z = 0.095 - 0.101$, however they are likely dying faint radio lobes, with no FIRST counterpart. Since there is no easy way to cross check all the different patches, we still computed the statistics for the most conservative scenario by assuming that the level of observed diffuse emission in excess of Im_{empty} is entirely due to the cosmic web. In this case, the level of confidence associated to the rejection of the same models loosens. However, the models rejected by casting hypothesis II are the same ones resulting from hypothesis I, though with slightly lower or even equal CL. (e.g. for the $B_0 = 30$ nG model the CL for its rejection decreases from 98% to 96% and all lower B_0 models remain unchanged. Furthermore, since hypothesis II has been falsified already by the examples described above and shown in Fig. 8, hypothesis I is strengthen in favor of hypothesis II and we thus refer to the former in order to draw our conclusions.

For completeness, a third additional and interesting way is instead the complementary hypothesis to the first one: we assume that at least some of the diffuse emission in excess of Im_{empty} comes from the cosmic web. The associated probabilities is then trivially $P(> P_S) = 1 - P(< P_S)$. In this case we are not interested in the level of diffuse emission in $Im_{diffuse}$, since we want to produce at least the one in Im_{empty}. This scenario, though disfavored, can not be discarded a priori since this would imply checking (e.g. through cross-correlations) all the different patches of diffuse emission in $Im_{diffuse}$ and prove that all of them are not connected to the emission from the Cosmic Web, it is then instructive to inspect its implications. Under the assumption that we did see the cosmic web emission at least in part, then the $B_0 = 0.1$ nG model is ruled out with high confidence $\geq 99\%$ since it is not able to produce any observable emission brighter than the noise level of our LOFAR observation. In this scenario, $B_0 > 0.1$ nG can be set as a lower limit to the primordial magnetic field intensity and in turn $B > 2$ nG as the median value for the magnetic field into filaments today.

While checking that the source injection procedure (presented in Sec. 2 and sketched in Fig. 1) is actually needed in order to derive robust limits on B_{Mpc} and B_0 we also demonstrate that the method is essential to interpret observations in details by means of the outcome of simulations when dealing with radio data. With this respect, we produced the same statistic P_S for the simulations directly added to the residual image Im_{empty} in terms of simple image sum, rather than following the central FFT + write + sum procedure involving visibilities. This procedure is much simpler and faster (shortening the computing time of a factor ~ 600). In Fig. 9 we plot the power spectra resulting from the injection in the RXC_J1659-J1702 field of one source as example (images of the same source are shown in Fig. 4) in order to inspect differences between the injection through the uvw- (black lines) and image-plane (grey lines), for the different B_0 models. As can be seen by comparing the black and gray lines, when the injection is performed within the image-plane the level of simulated emission at large scales is generally underestimated. As a consequence the models are consistent with the data with different probability up to $\pm 30\% P(< P_S)$ (see the values in Tab. 2). We interpret the difference in the results as due to the lack of model convolution with the instrument's Point Spread Function (PSF). In addition, the lack of convolution of the emission with a visibility weighting scheme able to maximise the evidence for extended diffuse emission into the data may also play a similar role. As far as an upper cut on the scales of the emission (corresponding to a lower bound on the baseline length in radio interferometers) is taken into account, and detailed power spectrum information does not constitute the largest budget of uncertainty in one analysis (in our case is the scatter in the properties of the -unknown- inter-cluster WHIM), the image sum is a much faster approach than the source injection through the uvw-plane, however it shall be used with caution as results are biased by a different sampling of the scales. The strength of the bias depends either on the sampling (window) function and the source power spectrum.

As a final caveat, our analysis assumes that for strong shocks in and around filaments, the acceleration efficiency of electrons is the one suggested by DSA, i.e. $\xi_e \sim 10^{-2}$. This assumes, in turn, that despite the rather low particle density and magnetisation, shocks can form and undergo particle acceleration similar to what is already observed for the outer regions of galaxy clusters in form of gaint radio relics (see van Weeren et al. 2019, for a review). Moreover, our analysis assumes that the acceleration of electrons at shocks can proceed independently on the obliquity between the upstream magnetic field and the shock normal. However, recent numerical works by Banfi et al. (2020) have shown that shocks surrounding the cosmic web are more often quasi-perpendicular than random chance, as an effect to the peculiar gas velocity flow following the formation of filaments. In this case, the vast majority of shocks in filaments are quasi-perpendicular and thus likely to be suitable for efficient electron acceleration (Xu et al. 2020). Furthermore, Masters et al. (2017) recently reported a significant electron acceleration by the strong quasi-parallel shock while crossing the Saturn bow shock by the Cassini space mission, i.e. in plasma conditions similar to the intracluster medium. The acceleration seems to occur in the portion of the shock where upstream cosmic-ray streaming instabilities generate perpendicular small-scale magnetic field components, leading to particle acceleration.
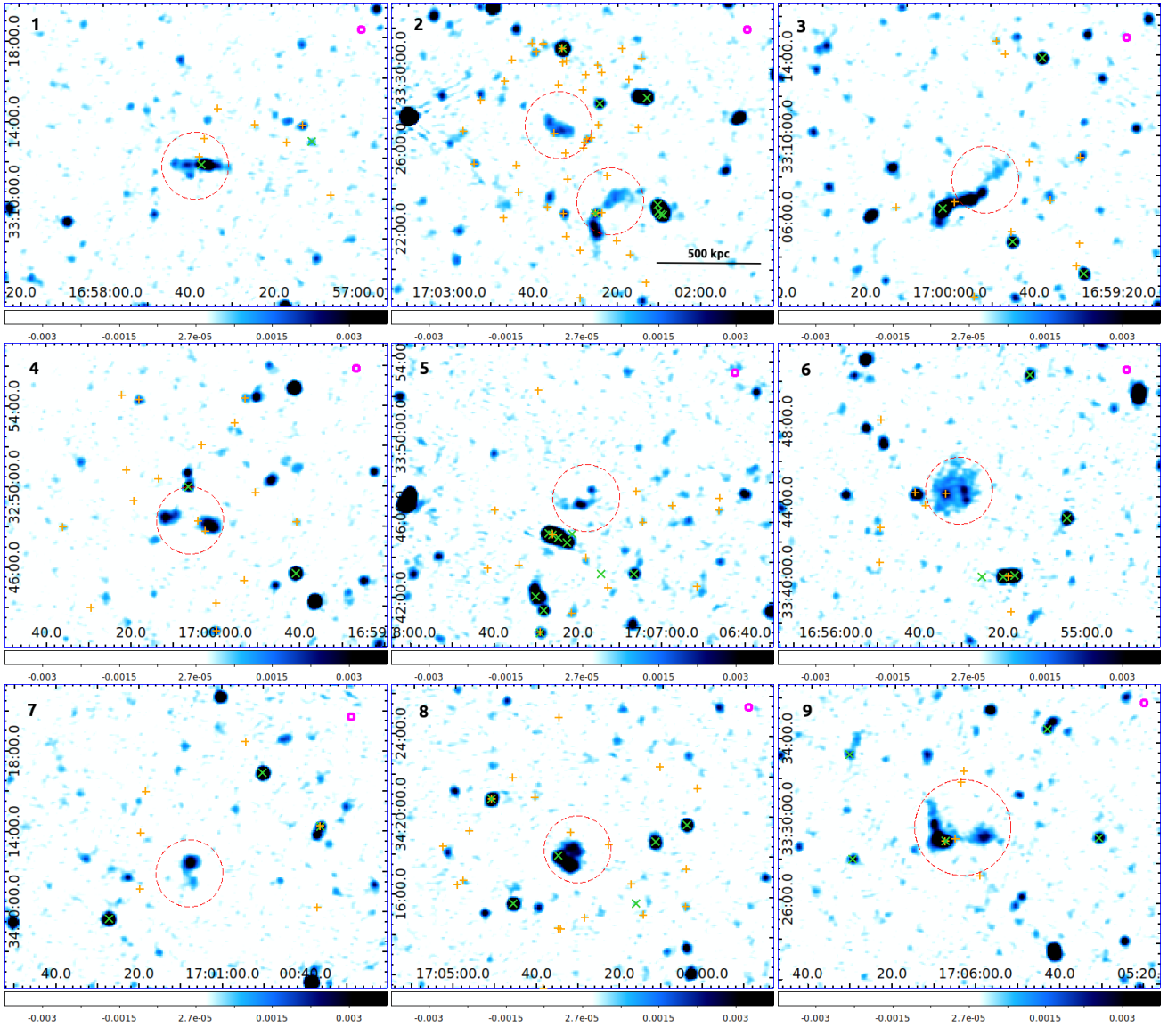
Figure 8. Zoom-in low resolution sky images (20″, see the magenta solid circles) centered over the patches of diffuse emission found in Im$_{\text{diffuse}}$ of RXC_J1659-J1702 as indicated by the dashed red circles. Green X symbols show the position of FIRST sources. Orange crosses show the position of SDSS galaxies with known spectroscopic redshift. Panels are numbered from 1 to 9 going from left to right and top to bottom. 1″ = 1.84 kpc at $z = 0.10$, we marked the 500 kpc scale in panel 2 for comparison. Colorbars are in Jy beam^{-1}.

5 CONCLUSIONS

In this work, we attempted for the first time to combine dedicated LOFAR-HBA observations of inter-cluster filaments and numerical simulations of the magnetic cosmic web, in order to derive upper limits on the magnetisation of the WHIM.

While our LOFAR observations do detect patches of diffuse emission of unclear origin their morphology does not allow us to firmly associate the origin of the most prominent ones to the cosmic web. However, the presence of a faint diffuse large scale excess in comparison with numerical models allows us to derive inferences on the average magnetisation of such filaments, and possibly on the allowed initial amplitude of primordial seed magnetic fields. As a main outcome of our work (following from assuming that our observations constitute *non-detections* of diffuse emission from the cosmic web and fixing $\xi_e = 0.01$ for strong shocks), we derive an upper limit for the median magnetic field strength in filaments con-

necting massive galaxy clusters: $B_{\text{Mpc}} < 0.2 - 0.6\,\mu\text{G}$, depending on whether future measurements will prove or exclude the presence of the WHIM between the observed cluster pairs. Based on the dynamical evolution of magnetic fields given by present simulations (which is mostly dominated by simple compression of magnetic field lines), this also implies an upper limit of $B_0 < 10 - 30$ nG on the amplitude of primordial seed fields.

As a mutually exclusive interpretation of our data, if some of the detected emission may partially come from the shocked WHIM, this would imply a median magnetic field of order of $B_{\text{Mpc}} \geq$ nG (see e.g. Fig. 6). This would be an important outcome as it would also possibly indicate primordial magnetic fields with intensity $B_0 \geq 0.1$ nG.

Given the uncertainties connected to our method and the limited statistics of "detections" in our sample, we propend for the first interpretation of our result.
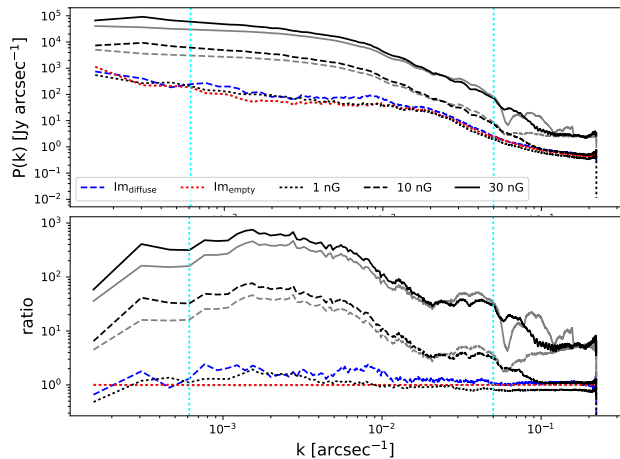
Figure 9. Power spectrum of the injected filament shown in Fig. 4 for different B_0 models, as labelled. The vertical cyan dotted lines show the integration scale limits used to compute P_S. They correspond respectively to about half the largest scale in the image $k^{-1} = 2173'' \sim 483$ pixels and $k^{-1} = 40''$ (corresponding to twice the synthesized beam FWHM scale). Black lines show $P(k)$ resulting from the source injection into uvw visibilities whereas grey lines show the result from the image-plane addition of the simulated image onto Im$_{empty}$. The lower panel shows the same power spectra as in the upper panel, divided by the Im$_{empty}$ line.

To put our new limits in comparison with other recent works (Hackstein et al. 2016; Pshirkov et al. 2016; Vernstrom et al. 2017; Brown et al. 2017; Vernstrom et al. 2019; O'Sullivan et al. 2020; Natwariya 2020, and Paoletti & Finelli 2019 for joint BICEP2/Keck - Planck 2018 updated results), we show them in Fig. 10 separating the limits inferred for the IGMF or the magnetic field intensity of the WHIM (red arrows) and for the primordial magnetic field intensity B_0 (blue arrows). We note that our limits are still in agreement with the recent limits $0.134 < B_0/\text{nG} < 0.316$ set by the level of excess diffuse emission observed by ARCADE2 and EDGES 21cm line experiments (Natwariya 2020). Furthermore, an apparent tension seems to arise between our lower limit to B_{Mpc} into filaments and the one derived from other probes such as the level of anisotropy in the arrival direction of charged ultra-high-energy cosmic rays used to limit the average amplitude of magnetic fields in voids to $\leq$ 1nG (Hackstein et al. 2016), or from the non-detection of a trend of rotation measures from distant radio sources with respect to redshifts (Pshirkov et al. 2016). Although computed over similar linear scales $\geq$ Mpc and globally refer to the IGM, they can still hardly be directly compared since referred to different IGM environments (e.g. voids, filaments, averaged). Interestingly a recent work has suggested that primordial magnetic fields with amplitude ~ 0.1 nG would possibly alleviate the existing tension between cosmological and standard candle-based estimates of H_0 (Jedamzik & Pogosian 2020).

While it is hard to derive conclusive limits from these data, as no robust detection (although tentative) of the diffuse emission from the cosmic web can be claimed, this first attempt stresses the potential of low-frequency radio observations in constraining extragalactic magnetic fields, and its relevance to the study of cosmic magnetogenesis. With the analysis and the values obtained in this work, we can forecast to produce tighter constraint than the ones posed by CMB experiments by covering a $\sim \times 10$ larger sample of cluster pairs similar to the ones analysed here even in the case of other non-detections.
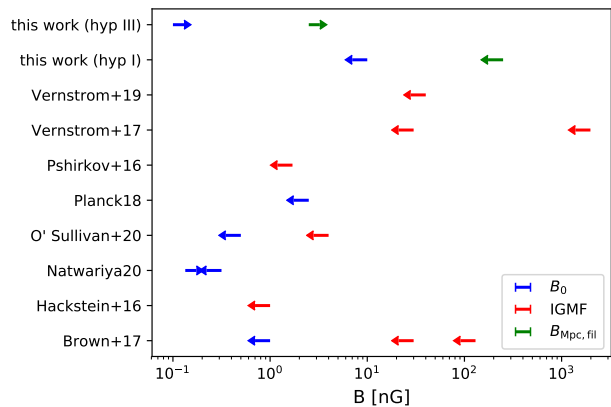
Figure 10. Summary of the current upper and lower limits to the volume-averaged IGMF (red arrows), B in the filaments' WHIM (green arrows) and B_0 (blue arrows).

6 DATA AVILABILITY

The code used to produce the simulations discussed in this paper is public (enzo-project.org). Significant subsets of the simulations are publicly available at https://cosmosimfrazza.myfreesites.net/the_magnetic_cosmic_web, while larger dataset can be shared upon request

REFERENCES

Aghanim N., et al., 2019, A&A, 632, A47

Akahori T., Gaensler B. M., Ryu D., 2014, ApJ, 790, 123

Banfi S., Vazza F., Wittor D., 2020, MNRAS, 496, 3648

Becker R. H., White R. L., Helfand D. J., 1995, ApJ, 450, 559

Beresnyak A., Miniati F., 2016, ApJ, 817, 127

Botteon A., et al., 2020a, arXiv e-prints, p. arXiv:2008.09613

Botteon A., Brunetti G., Ryu D., Roh S., 2020b, A&A, 634, A64

Briggs D. S., 1995, in American Astronomical Society Meeting Abstracts. p. 112.02

Brown S., et al., 2017, MNRAS, 468, 4246

Brüggen M., Ruszkowski M., Simionescu A., Hoeft M., Dalla Vecchia C., 2005, ApJ, 631, L21

Bryan G. L., et al., 2014, ApJS, 211, 19

Bykov A. M., Vazza F., Kropotina J. A., Levenfish K. P., Paerels F. B. S., 2019a, Space Sci. Rev., 215, 14

Bykov A. M., Petrov A. E., Krassilchtchikov A. M., Levenfish K. P., Osipov S. M., Pavlov G. G., 2019b, ApJ, 876, L8

Cen R., Ostriker J. P., 1999, ApJ, 514, 1

Colberg J. M., Krughoff K. S., Connolly A. J., 2005, MNRAS, 359, 272

Davé R., et al., 2001, ApJ, 552, 473

Dedner A., Kemm F., Kröner D., Munz C. D., Schnitzer T., Wesenberg M., 2002, Journal of Computational Physics, 175, 645

Dolag K., Bartelmann M., Lesch H., 1999, A&A, 348, 351

Donnert J., Vazza F., Brüggen M., ZuHone J., 2018, Space Sci. Rev., 214, 122

Gheller C., Vazza F., Bonafede A., 2018, MNRAS, 480, 3749

Govoni F., et al., 2019, Science, 364, 981

Hackstein S., Vazza F., Brüggen M., Sigl G., Dundovic A., 2016, MNRAS, 462, 3660

Hoeft M., Brüggen M., 2007, MNRAS, 375, 77

Jedamzik K., Pogosian L., 2020, arXiv e-prints, p. arXiv:2004.09487

Kang H., Ryu D., Jones T. W., 2012, ApJ, 756, 97

Locatelli N., Vazza F., Domínguez-Fernández P., 2018, Galaxies, 6, 128

Macquart J. P., et al., 2020, Nature, 581, 391

Masters A., et al., 2017, ApJ, 843, 147

Mechev A., Oonk J. B. R., Danezi A., Shimwell T. W., Schrijvers C., Intema H., Plaat A., Rottgering H. J. A., 2017, in Proceedings of the International Symposium on Grids and Clouds (ISGC) 2017. p. 2 (arXiv:1712.00312)

Mohan N., Rafferty D., 2015, PyBDSF: Python Blob Detection and Source Finder (ascl:1502.007)

Natwariya P. K., 2020, arXiv e-prints, p. arXiv:2007.09938

Nicastro F., et al., 2018, Nature, 558, 406

O'Sullivan S. P., et al., 2020, MNRAS, 495, 2607

Offringa A. R., et al., 2014, MNRAS, 444, 606

Paoletti D., Finelli F., 2019, J. Cosmology Astropart. Phys., 2019, 028

Piffaretti R., Arnaud M., Pratt G. W., Pointecouteau E., Melin J. B., 2011, A&A, 534, A109

Pshirkov M. S., Tinyakov P. G., Urban F. R., 2016, Phys. Rev. Lett., 116, 191302

Ryu D., Kang H., Cho J., Das S., 2008, Science, 320, 909

Shimwell T. W., et al., 2017, A&A, 598, A104

Shimwell T. W., et al., 2019, A&A, 622, A1

Smirnov O. M., Tasse C., 2015, MNRAS, 449, 2668

Stuardi C., et al., 2019, MNRAS, 489, 3905

Stuardi C., et al., 2020, A&A, 638, A48

Tasse C., 2014a, arXiv e-prints, p. arXiv:1410.8706

Tasse C., 2014b, A&A, 566, A127

Tasse C., et al., 2018, A&A, 611, A87

Uchiyama Y., Aharonian F. A., Tanaka T., Takahashi T., Maeda Y., 2007, Nature, 449, 576

Vacca V., et al., 2016, A&A, 591, A13

Vazza F., Brüggen M., Gheller C., Wang P., 2014, MNRAS, 445, 3706

Vazza F., Ferrari C., Brüggen M., Bonafede A., Gheller C., Wang P., 2015, A&A, 580, A119

Vazza F., Brüggen M., Gheller C., Hackstein S., Wittor D., Hinz P. M., 2017, Classical and Quantum Gravity, 34, 234001

Vazza F., Ettori S., Roncarelli M., Angelinelli M., Brüggen M., Gheller C., 2019, A&A, 627, A5

Vernstrom T., Gaensler B. M., Brown S., Lenc E., Norris R. P., 2017, MNRAS, 467, 4914

Vernstrom T., Gaensler B. M., Rudnick L., Andernach H., 2019, ApJ, 878, 92

Williams W. L., et al., 2016, MNRAS, 460, 2385

Xu R., Spitkovsky A., Caprioli D., 2020, ApJ, 897, L41

de Gasperin F., et al., 2019, A&A, 622, A5

van Weeren R. J., et al., 2016, ApJS, 223, 2

van Weeren R. J., de Gasperin F., Akamatsu H., Brüggen M., Feretti L., Kang H., Stroe A., Zandanel F., 2019, Space Sci. Rev., 215, 16

This paper has been typeset from a TEX/LATEX file prepared by the author.